OrBITS: Label-free and time-lapse monitoring of patient derived organoids for advanced drug screening.

Authors: Christophe Deben[1*], Edgar Cardenas De La Hoz[2]*, Maxim Le Compte[1], Paul Van Schil[3], Jeroen M. Hendriks[3], Patrick Lauwers[3], Suresh Krishan Yogeswaran[3], Filip Lardon[1], Patrick Pauwels[1,4], Steven Van Laere[1], Annemie Bogaerts[6], Evelien Smits[1,5], Steve Vanlanduit[2], Abraham Lin[1,6]

*Both authors contributed equally to the manuscript. Christophe Deben for the biological part, Edgar Cardenas De La Hoz for the computational part.

1. Center for Oncological Research (CORE), Integrated Personalized & Precision Oncology Network (IPPON), University of Antwerp, Wilrijk, Belgium.

2. Industrial Vision Lab, University of Antwerp, Groenenborgerlaan 171, Antwerp 2020, Belgium

3. Department of Thoracic and Vascular surgery, Antwerp University Hospital, Edegem, Belgium.

4. Department of Pathology, Antwerp University Hospital, Edegem, Belgium.

5. Center for Cell Therapy and Regenerative Medicine, Antwerp University Hospital, Edegem, Belgium.

6. Plasma Lab for Applications in Sustainability and Medicine ANTwerp (PLASMANT), University of Antwerp, 2610 Wilrijk, Belgium.

Corresponding author: christophe.deben@uantwerpen.be

25 **Abstract**

26 **Background:** Patient-derived organoids are invaluable for fundamental and translational cancer
27 research and holds great promise for personalized medicine. However, the shortage of available
28 analysis methods, which are often single-time point, severely impede the potential and routine use
29 of organoids for basic research, clinical practise, and pharmaceutical and industrial applications.

30 **Methods:** Here, we developed a high-throughput compatible and automated live-cell image
31 analysis software that allows for kinetic monitoring of organoids, named **Or**ganoid **B**rightfield
32 **I**dentification-based **T**herapy **S**creening (OrBITS), by combining computer vision with a
33 convolutional network machine learning approach. The OrBITS deep learning analysis approach
34 was validated against current standard assays for kinetic imaging and automated analysis of
35 organoids. A drug screen of standard-of-care lung and pancreatic cancer treatments was also
36 performed with the OrBITS platform and compared to the gold standard, CellTiter-Glo 3D assay.
37 Finally, the optimal parameters and drug response metrics were identified to improve patient
38 stratification.

39 **Results:** OrBITS allowed for the detection and tracking of organoids in routine extracellular
40 matrix domes, advanced Gri3D®-96 well plates, and high-throughput 384-well microplates, solely
41 based on brightfield imaging. The obtained organoid Count, Mean Area, and Total Area had a
42 strong correlation with the nuclear staining, Hoechst, following pairwise comparison over a broad
43 range of sizes. By incorporating a fluorescent cell death marker, intra-well normalization for
44 organoid death could be achieved, which was tested with a 10-point titration of cisplatin and
45 validated against the current gold standard ATP-assay, CellTiter-Glo 3D. Using this approach with
46 OrBITS, screening of chemotherapeutics and targeted therapies revealed further insight into the

mechanistic action of the drugs, a feature not achievable with the CellTiter-Glo 3D assay. Finally, we advise the use of the growth rate-based normalised drug response metric to improve accuracy and consistency of organoid drug response quantification.

Conclusions: Our findings validate that OrBITS, as a scalable, automated live-cell image analysis software, would facilitate the use of patient-derived organoids for drug development and therapy screening. The developed wet-lab workflow and software also has broad application potential, from providing a launching point for further brightfield-based assay development to be used for fundamental research, to guiding clinical decisions for personalized medicine.

Keywords: patient-derived organoids, drug screening, high-throughput, image-based analysis

1. Introduction

The use of 2D cancer cell lines has traditionally been the gold standard in preclinical *in vitro* cancer research. However, these models fail to recreate the complex cell-cell interactions present in the tumor microenvironment and lack the genetic heterogeneity found in cancer patients. In addition, prolonged use of these cancer cell lines leads to acquired mutations or gene expression alterations, which are often overlooked as the cell line deviates from the originally derived tumor. As a result, new therapies are often met with high failure rates during translation from preclinical research to clinical trials, thus resulting in extreme forfeiture of research labor and financial loss.

The development of 3D cell culture technologies has greatly improved the physiological relevance of *in vitro* cancer models and the use of patient-derived organoids (PDOs) is revolutionizing basic and translation cancer research (1). These PDOs resemble both the pheno- and genotype of the

69 tissue they are derived from and can be expanded long-term and cryopreserved to establish a living
70 tumor and healthy tissue biobank (1). Furthermore, one of the most promising applications of
71 PDOs is for personalized cancer treatment to predict clinical response *ex vivo* (2-8). However, the
72 available repertoire of assays for high-throughput organoid analysis is severely limited, and
73 therefore, the current gold standard relies on a rudimentary viability assay.
74 The gold standard analysis method, Promega CellTiter-Glo 3D cell viability assay, determines the
75 number of viable cells in 3D cell cultures based on luminescent quantification of intracellular ATP
76 in both 96- and 384-well microplate format. This method is met with several intrinsic limitations
77 including inter-patient growth rate variations and (drug-induced) metabolic modulations, which
78 could affect the translatability of this readout (9-11). For drug screening and diagnostic
79 applications, this assay is also unable to determine the mechanistic action of the drug, such as
80 cytostatic or cytotoxic response, and is limited to a single time-point analysis. These aspects
81 critically limit the wide adoption of organoid technology for clinical diagnostics and
82 pharmaceutical drug screening. Therefore, although the CellTiter-Glo viability assay has been a
83 valuable method to monitor drug responses, more sophisticated high-throughput analysis methods
84 are urgently needed.
85 In this study, we addressed these shortcomings by using an automated, high-throughput
86 compatible, and kinetic screening platform to monitor therapy response. Using the Tecan Spark
87 Cyto multi-mode plate reader system, we automated seeding of full-grown PDOs in a 384-well
88 format and performed real-time, whole-well brightfield (BF) and fluorescence imaging in a
89 temperature, CO_2, and O_2 controlled environment. This reduces the variability involved in manual
90 organoid cultures, which is highly cumbersome and not scalable. Using our in-house developed

91 OrBITS (**Or**ganoid **B**rightfield **I**dentification-based **T**herapy **S**creening) live-cell image analysis
92 software, which utilizes convolutional network machine learning to eliminate the use of
93 fluorescent live-cell labelling dyes, we validated the capacity for BF imaging-based monitoring of
94 PDO growth, by comparing our results to the current industry and research standards. The
95 combination of BF imaging with a fluorescent cell death marker further demarcated cytostatic
96 from cytotoxic therapy responses, thus providing greater insight into drug effects and the potential
97 for improving translation into a durable clinical response in patients. Using this automation setup
98 and OrBITS, we performed a screening of several chemotherapeutics and targeted therapies on
99 patient-derived organoids as a proof-of-concept and identified the most suitable drug response
100 metric. The technology described here to produce and validate our wet-lab workflow and image
101 analysis software unlocks the potential for wide adoption of organoid-based assays for drug
102 screening and discovery as well as guidance of clinical decision for personalized medicine.

103 ## 2. Materials and Methods

104 ### 2.1 Patient tissue

105 Tumor tissue and normal lung tissue (distant from the tumor site) were obtained from adeno- and
106 squamous cell carcinoma non-small cell lung carcinoma (NSCLC) and pancreatic ductal
107 adenocarcinoma patients undergoing curative surgery at the Antwerp University Hospital (UZA)
108 in 2019-2021. Written informed consent was obtained from all patients, and the study was
109 approved by the UZA Ethical Committee (ref. 17/30/339; 14/47/480). All samples were registered
110 in the Biobank Antwerp, Belgium; ID: BE 71030031000. Mutation analysis on the parental
111 NSCLC tissue was performed as part of standard-of-care using the Oncomine Focus Assay
112 (Thermo Fisher Scientific) at the UZA pathology department.

113 **2.2 Tissue processing and organoid culture**

114 Tissue was stored in Ad-DF+++ (Advanced DMEM/F12 (GIBCO), with 1% GlutaMAX
115 (GIBCO), 1% HEPES (GIBCO), 1% penicillin/streptomycin (GIBCO) supplemented with 2%
116 Primocin (Invivogen) at 4°C and transported on ice to be processed within 24 hours for organoid
117 culture. Tumor and normal tissue were minced with two scalpels, collected in 0.1% BSA precoated
118 tubes and washed with PBS. Next, fragments were dissociated with 0.5 mg/mL dispase type II
119 (Sigma-Aldrich), 1.5 – 5 mg/mL collagenase type II (Sigma-Aldrich), 1:500 Primocin and 10 µM
120 Y-27632 (Cayman Chemicals) in MG^{2+}/Ca^{2+} PBS (GIBCO) for 60 minutes at 37°C. Digested cells
121 were washed three times with PBS and resuspended in 2/3 Cultrex Type 2 (R&D Systems) and
122 1/3 Full Ad-DF+++ medium and plated in drops which were allowed to solidify for 30 minutes at
123 37°C after which they were overlayed with Full Ad-DF+++ medium. Full lung Ad-DF+++
124 medium consisted of 10% Noggin conditioned medium (HEK293-mNoggin-Fc; kindly provided
125 by Hans Clever, Hubrecht Institute), 10% R-spondin-1 conditioned medium (293T-HA-Rspol-Fc;
126 kindly provided by Calvin Kuo, Stanford University), 1 x B27 supplement (GIBCO), 10 mM
127 nicotinamide (Sigma-Aldrich), 25 ng/mM human recombinant FGF-7 (Peprotech), 100 ng/mL
128 human recombinant FGF-10 (Peprotech), 500 nM A83-01 (Tocris), 1 µM SB202190 (Cayman
129 Chemicals) and 5 µM Y-27632 (only used after passaging and thawing). Full PDAC Ad-DF+++
130 medium consisted of 0.5nM WNT Surrogate-Fc-Fusion protein (Immunoprecise), 4% Noggin-Fc
131 Fusion Protein conditioned medium (Immunoprecise), 4% Rspo3-Fc Fusion Protein conditioned
132 medium (Immunoprecise), 1x B27 without vitamin A, 10 mM nicotinamide, 100 ng/ml FGF-10,
133 500 nM A83-01, 10 nM gastrin (R&D Systems) and 5 mM Y-27632.

134 For passaging, organoids were digested to single cells with TrypLE Express (GIBCO). For
135 cryopreservation, 3-day old organoids were harvested with Cultrex Harvesting Solution (R&D
136 Systems) and frozen in Recovery Cell Culture Freezing Medium (GIBCO). Samples were tested
137 for Mycoplasma contamination with the MycoAlert Mycoplasma Detection Kit (LONZA).

138 **2.3 Immunohistochemical analysis**

139 Early passage organoids were collected using Cultrex Organoid Harvesting Solution (R&D
140 systems), washed with ice-cold PBS, and fixated in 4% paraformaldehyde for 30 minutes at room
141 temperature. Fixed organoids were transferred to a 4% agarose micro-array mold and paraffin-
142 embedded as described before (12). Five µm-thick sections were prepared, deparaffinized and
143 rehydrated prior to staining. Sections were subjected to heat-induced antigen retrieval by
144 incubation in a low pH buffer (Envision Flex TRS low pH (DAKO) for 20 min at 97°C (PT-Link,
145 DAKO). Endogenous peroxidase activity was quenched by incubation in peroxidase blocking
146 buffer (DAKO) for 5 min. Slides were stained manually with mouse anti-TTF1 (clone SPT24;
147 TTF-1-L-CE, Leica, 1/400, 25') and mouse anti-P40 (clone BC28; Cat# ACI 3066 A, C,
148 RRID:AB_2858274, Biocare, ready-to-use, 30') primary antibodies followed by an incubation
149 with ENVISION Flex+ Mouse Linker (DAKO, 15') for signal amplification. Mouse anti-NapsinA
150 (clone MRQ-60, Cell Marque, 1/350, 35') staining was performed on a DAKO autostainer Link
151 48. After that the slides were incubated for 25 min with Envision FLEX/HRP (ready-to-use,
152 DAKO) secondary antibody followed by 10 min incubation with the DAB substrate/chromogen
153 detection system (DAKO). The sections were counterstained for 2 min with hematoxylin (0.1%),
154 dehydrated and mounted with Quick-D Mounting Medium (KliniPath). Sections were imaged
155 using a Leica DM500 microscope equipped with an ICC50 E camera.

156 **2.4 In vitro drug screening**

157 Three days before the start of the experiment, organoids were passaged as single cells using
158 TrypLE and plated in Cultrex drops. Subsequently, organoids were harvested with Cultrex
159 Harvesting Solution, collected in 15 mL tubes coated with 0.1% BSA/PBS, washed with Ad-
160 DF+++ and resuspended in 1 mL Full Ad-DF+++ medium (without Y-27632). Next the number
161 of organoids were counted with the Sceptor 2.0 using a 60 µM sensor (Merck Millipore).
162 Organoids were then diluted in Full Ad-DF+++ and 5% Cultrex on ice to a concentration that
163 results in 500-2000 organoids/60µL. 60µL of this solution was plated into a 384-well ultra-low
164 attachment microplate (Corning, #4588) using the Tecan Spark Cyto Injector at a speed of 100
165 µL/s to avoid bubbles. All tubes and the Spark Cyto Injector were primed with 0.1 % BSA/PBS to
166 avoid sticking of the organoids. Next, the plate was centrifuged (100 rcf, 30 sec, 4°C) and
167 incubated for at least 30 minutes at 37°C.

168 All drugs and fluorescent reagents were added to the plate using the Tecan D300e Digital
169 Dispenser. Cytotox Green (75 nM / well, Sartorius), Caspase 3/7 Green Reagent (2.5 µM / well,
170 Sartorius), Z-VAD-FMK (50 µM / well, Bachem AG), Erlotinib, Gefitinib, Osimertinib and
171 Afatinib (Selleckchem) were dissolved in DMSO. Hoechst 33342 (50 nM / well, ThermoFisher),
172 Cisplatin (Tocris) and Carboplatin (Selleckchem) were dissolved in PBS to yield a final
173 concentration of 0.3 Tween-20 required for dispensing with the D300e Dispenser.

174 BF, green and blue fluorescence whole-well images (4x objective) were taken with the Tecan
175 Spark Cyto set at 37°C / 5% CO_2 for kinetic experiments in a humidity cassette. For endpoint
176 measurement of ATP levels, 60 µL CellTiter-Glo 3D reagent (Promega) was injected using the

177 Tecan Spark Cyto Injector to each well, shaken for 5 minutes and measured after 30 minutes
178 incubation with the Tecan Spark Cyto luminescence module.
179 A detailed video protocol will be made available in the Journal of Visualized Experiments (13).

180 **2.5 Drug response metrics**

181 Dose-response curves were plotted and IC_{50}-values were calculated using GraphPad Prism 9
182 (GraphPad Prism, RRID:SCR_002798). Drug concentrations were transformed to log10 and raw
183 data results were normalized to vehicle (100%) and/or baseline control (0%) (Staurosporin 5 µM
184 or 100 µM cisplatin) for viability assessment, and vice versa for cell death assessment (EC_{50}).
185 Curves were fitted using the log (inhibitor/agonist) vs. normalized response - Variable slope
186 function.
187 The growth rate (GR) metric (negative control) and the normalized drug response (NDR) metric
188 (positive and negative controls) were calculated based on the work of Hafner and colleagues (14)
189 and Gupta and colleagues (15), respectively, using the adapted R script from Gupta et al.. The
190 Total BF Area – Total Green Area parameter was used, and the fold change was calculated for
191 each well individually from the first measurement (T0) and a timepoint as indicated in the figures.
192 Based on the NDR values, the drug effects can be classified as: >1, proliferative effect; = 1, normal
193 growth as in negative control; = 0, complete growth inhibition; = -1, complete killing.
194 Screen quality was determined by calculating the Z Factor score using the formula (16):

195 $$1 - \frac{3 * SD\ (negative\ control) + 3 * SD\ (positive\ control)}{average\ (negatrive\ control) - average\ (positive\ control)}$$

196 **2.6 Image-based analysis**

197 Following image acquisition with the Tecan Spark Cyto, BF and fluorescence images were
198 analyzed using an in-house developed analysis software OrBITS. Briefly, a fully convolutional

199 network was used to take single images and return sematic segmentation maps as outputs. The
200 model training methodology was performed by using fluorescence intensity images as ground
201 truth. A detailed description about the image analysis and training methodology is provided in
202 Supplementary Information. An image mask, a colored overlay of identified objects, is applied to
203 visualize the accuracy of the image segmentation. The analysis output from OrBITS (Table S1)
204 was correlated with the current gold standard assays: Hoechst staining (for organoid tracking),
205 Cytotox Green (for organoid death), and the CellTiter-Glo 3D assay (for drug screening). Use of
206 the OrBITS image analysis software we developed is available to researchers upon reasonable
207 request and discussion with the corresponding author. In addition, a web-based platform is
208 currently being developed to increase accessibility of the software to users. Interest in this platform
209 can be expressed to the corresponding author.

210 **2.7 Organoid mutation analysis**

211 Full grown organoids were collected as described above and DNA was isolated using the QIAamp
212 DNA blood mini kit (Qiagen) and send to Genewiz Europe (Leipzig, Germany) for whole exome
213 sequencing on an Illumina NovaSeq platform (2 x 150 bp sequencing, 12Gb (120x)). Raw reads
214 were mapped onto the human reference genome (hg38) using the *BWA MEM* algorithm (v.0.7.17)
215 in standard settings. Resulting SAM-files were converted into BAM-files, coordinated-sorted, and
216 indexed using *samtools* (v.1.9). Reads overlapping with 86 genes mutated in at least 10% of either
217 PDAC or NSCLC samples included in the cBioPortal for cancer genomics were selected using the
218 *bedtools* (v.2.29.2) intersect-command retaining the full read in the original BAM-file (-wa
219 option). Variants were called using the haplotype-based variant detector freebayes (v.1.3.2;
220 Garrison E, Marth G. Haplotype-based variant detection from short-read sequencing. arXiv

221 preprint arXiv:1207.3907 [q-bio.GN] 2012) in standard settings and indel positions were left-
222 aligned and normalized using the *bcftools* (v.1.9) norm-command. Resulting VCF-files were
223 annotated using *SnpEff* (v.5.1) for functional annotations and *SnpSift* (v.5.1) for human genetic
224 variation using dbSNP (build 154), ClinVar (release 05/09/2022) and COSMIC (v96). Annotated
225 VCF files were further manipulated using the *SnpSift* filter-command retaining only coding, non-
226 synonymous variants that are contained COSMIC, that are not considered as benign and/or likely
227 benign by ClinVar, that have a minimal coverage of 120x with at least 40 reads supporting the
228 alternate allele with no positional or strand bias, that are not of germline origin or are reported as
229 common variants (minor allele frequency>1%) in any human population and that are either
230 missense, stop gained or frame shift mutations. Mutational profiles were visualized in oncoprint
231 format.

232 **2.8 Statistical Analysis**

233 Correlations were measured and visualized using linear fit regression using the least squares
234 approximation. The equation reports slope and bias between the two measured values as well as
235 the R squared value. Log IC50-values were compared using the extra sum-of-squares F test in
236 GraphPad Prism with a significance cut-off of $p < 0.05$.

237 **3. Results**

238 **3.1 Establishment of patient-derived organoids**

239 Validation of the organoid monitoring ability using BF imaging was performed on various lung
240 organoid lines. Organoids derived from NSCLC patient tumor resection fragments had a
241 predominantly solid growth pattern, while organoids derived from distant healthy lung tissue
242 displayed a cystic growth pattern (Fig. S1). Further immunohistochemical characterization of the

243 tumor tissue-derived organoids indicated that the cells were non-malignant and most likely
244 represent metaplastic squamous epithelial cells as suggested by Dijkstra and colleagues (details in
245 supplementary information, Fig. S1 and Table 1) (17, 18). This was further confirmed genetically,
246 since NSCLC_006T and NSCLC_013T organoids lack the KRAS and EGFR mutation found in
247 the parental tumor, respectively (Fig. S2, Table 1). These observations confirmed the challenges
248 related to generating pure NSCLC organoids. However, for validation of organoid monitoring with
249 OrBITS, these non-malignant organoids were equally relevant. The cystic NSCLC_006N and
250 NSCLC_051N organoids and solid NSCLC_013T, NSCLC_046T and NSCLC_051T organoids
251 were used in the subsequent experiments. In addition, the KRAS mutant PDAC_052 and
252 PDAC_060 lines were included as genetically validated tumor organoids (Fig. S2, Table 1).

Table 1: Overview of patient-derived organoid lines

Sample	Source	Morphology	Napsin A	P40	TTF1	Mutation Parental Tumor	Mutation in Organoids	Organoids
NSCLC_006N	Normal	Cystic	-/-	+/- (polarized)	+/+	NA	NA	Normal
NSCLC_006T	AC	Solid/Cystic	-/-	+/- (polarized)	+/+	KRAS c.34G<T	No	Non-malignant
NSCLC_013N	Normal	Cystic	+/-	+/- (polarized)	+/+	NA	NA	Normal
NSCLC_013T	AC	Solid	-/-	+/- (polarized)	+/+	EGFR c.2573T>G	No	Non-malignant
NSCLC_046N	Normal	Cystic	-/-	+/- (polarized)	+/+	NA	NA	Normal
NSCLC_046T	AC	Solid	-/-	+/+	+/+	No	No	Non-malignant
NSCLC_051N	Normal	Cystic	-/-	+/- (polarized)	+/+	NA	NA	Normal

NSCLC_051T	SQ	Solid	-/-	+/- (polarized)	+/+	No	No	Non-malignant
PDAC_052	AC	Cystic	NA	NA	NA	NA	KRAS c.34G>T	Tumoral
PDAC_060	AC	Cystic	NA	NA	NA	NA	KRAS c.35G>A	Tumoral
NSCLC: non-small cell lung cancer; PDAC: pancreatic ductal adenocarcinoma; AC: adenocarcinoma; SQ: squamous cell carcinoma; NA: not applicable.								

253

254 **3.2 Validation of label-free Brightfield monitoring of all stages of organoid growth**

255 A kinetic image set was generated from a serial dilution of single cells and 3-day old organoids
256 grown in a 384-well microplate from two organoid lines (NSCLC_013T and NSCLC_006N)
257 stained with Hoechst as a gold standard reference method. Pairwise comparison showed a strong
258 correlation of the organoid Count, Mean Area, and Total Area detected by BF when compared to
259 Hoechst for the entire range of organoid sizes (Fig. 1A). This indicates that OrBITS is capable of
260 kinetic monitoring at all stages of organoid growth in the absence of a fluorescent dye and based
261 solely on BF image analysis (Fig. 1B, Supplemental Video 1-3). For Mean and Total Mask Area,
262 BF analysis resulted in a higher area compared to Hoechst analysis, mainly in the cystic
263 NSCLC_006N line since Hoechst only identifies the edge of cystic organoids (Fig. 1A-B).

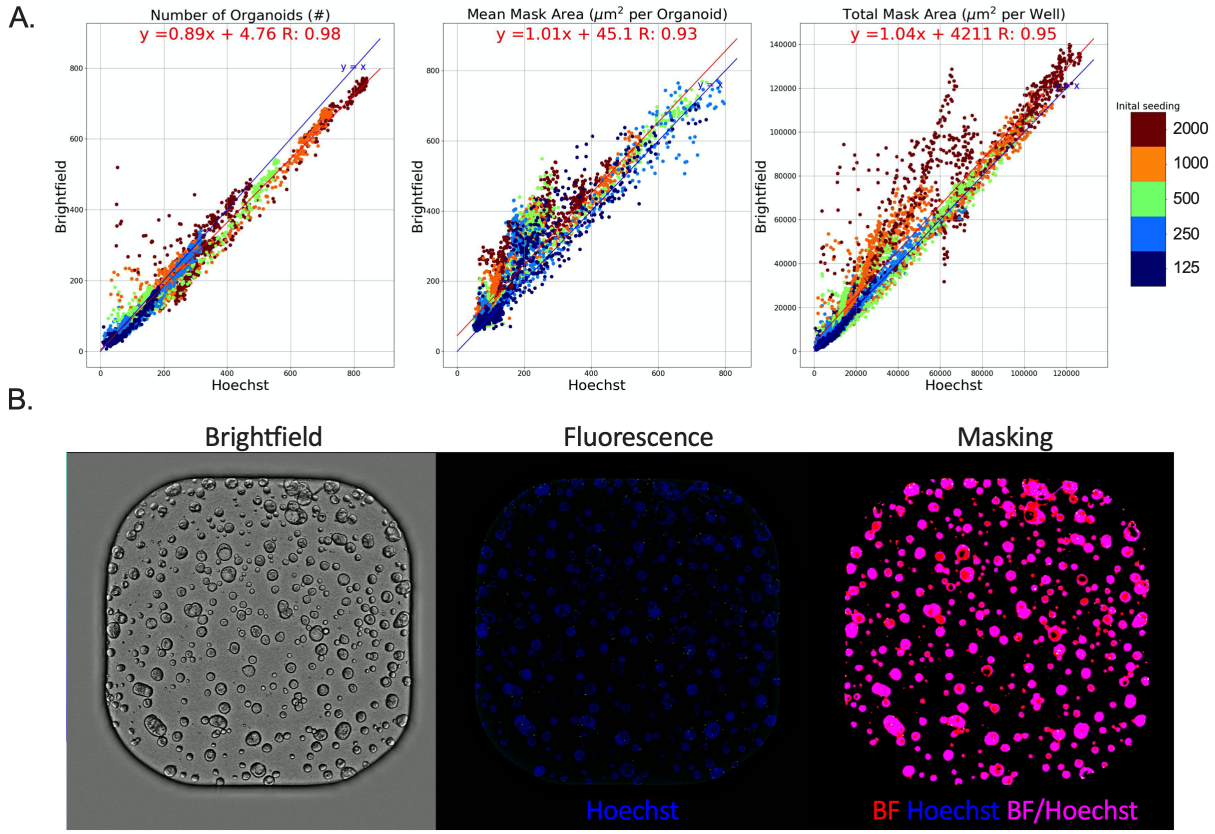

Figure 1: Brightfield versus Hoechst. (A) Pairwise comparison of organoid Counts, Mean Mask Area and Total Mask Area detected by Brightfield- and Hoechst-based analysis of NSCLC_013T and NSCLC_006N PDO lines plated as a serial dilution of single cells and 3-day old organoids (Table S2). Blue line: line of unity (x=y), red line: best-fit linear regression. (B) Representative whole 384-well brightfield and fluorescent images of full-grown PDOs (NSCLC_006N) and the corresponding analysis mask. Supplemental Video 3 presents the corresponding time-laps video.

Both organoid lines could be grown from either single cells (Fig. 2A) or fully-grown organoids, which are more conventionally used (Fig. 2B). An important advantage of the proposed assay is that growth kinetics can be accurately monitored using only a limited amount of starting material. In fact, using a larger number of single cells or organoids affected BF image monitoring results in two ways: (i) when both lines (NSCLC_013T and NSCLC_006N) were plated at high single cell densities, a drop in counts was observed over time due to organoids merging or fusion events (Fig. 2C-D, Supplemental Video 1) resulting in an aberrant growth rate based on Mean Area for

279 NSCLC_013T at higher seeding densities (Fig. 2A); (ii) NSCLC_006N PDOs showed a higher
280 growth rate compared to NSCLC_013T PDOs due to differential nutrient requirements. At higher
281 concentrations (>500 counts), we clearly observed a drop in NSCLC_006N organoids growth rate
282 compared to the slower growing NSCLC_013T organoids (Fig. 2B).

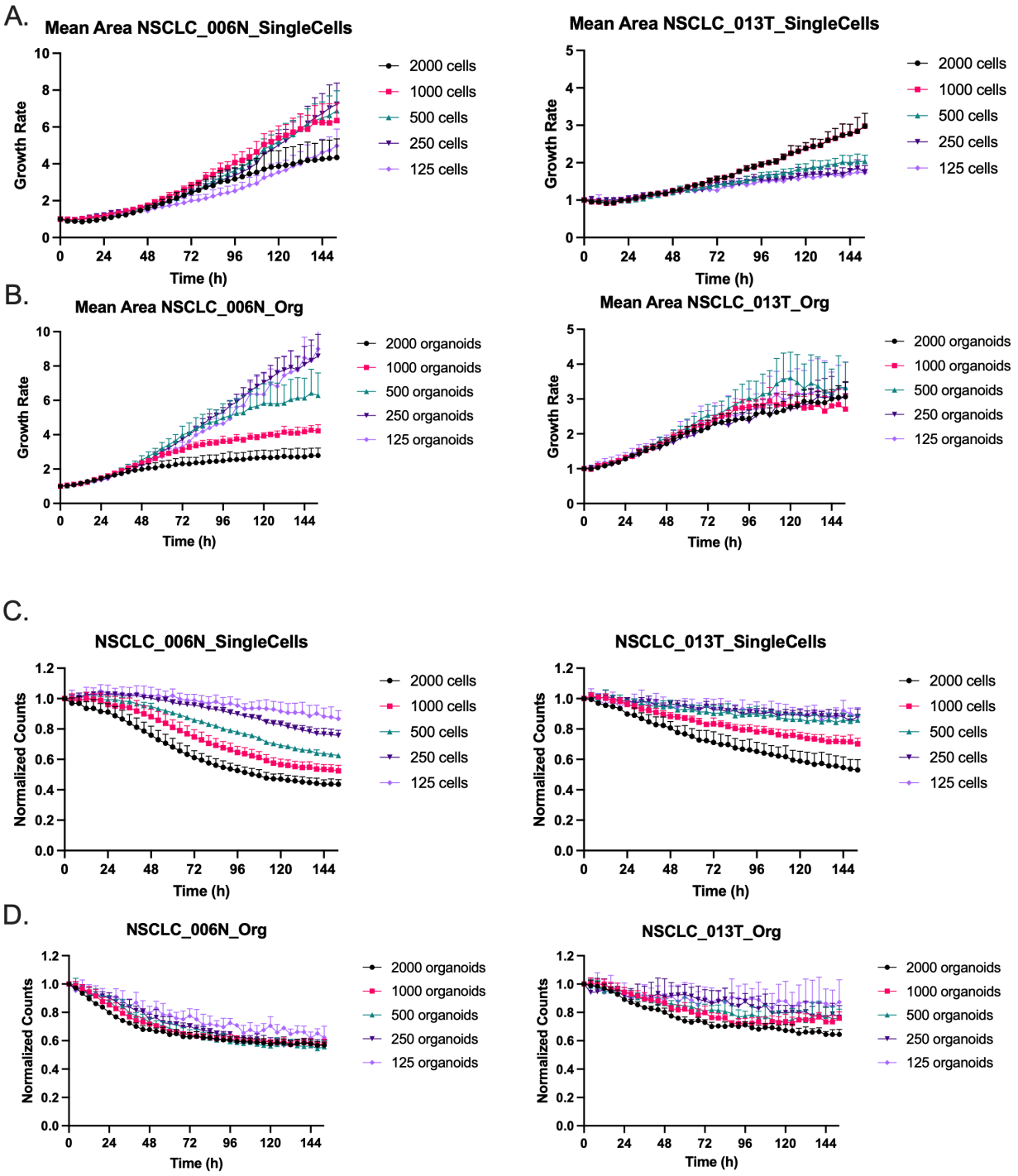

Figure 2: Influence of seeding density. Average growth rate of PDOs seeded as (A) single cells or (B) 3-day old organoids. Normalized counts (h=0) of PDOs seeded as (C) single cells or (D) 3-day old organoids. A range between 125 – 2000 cells or organoids were plated. Graphs presented as mean ± SD of 5 technical replicates and images were acquired every 6 hours.

288 **3.3 Monitoring organoid death with intra-well normalization**

289 Since PDOs used in drug screening will undergo varying degrees and stages of death, it is critical
290 that the OrBITS software is able to detect such organoids. Therefore, a second kinetic image set
291 was generated from two additional organoid lines to increase variation (NSCLC_051T and
292 NSCLC_051N; 500/well plated as 2-day old organoids) and treated with a 10-point titration of
293 cisplatin. PDOs were stained with Hoechst as the gold standard reference method and used for
294 validation of BF image analysis. Despite varying levels of cytotoxicity from the chemotherapeutic
295 treatment, the data showed that organoids were successfully identified from BF images (Fig. S3).
296 Importantly, common artefacts (e.g. air-bubbles, extracellular matrix, dust) did not disrupt BF
297 analysis (Fig. S3).

298 To further develop the applicability of the OrBITS software, we investigated the capacity for intra-
299 well normalization of organoid death with cell death markers, such as Cytotox Green. Since
300 Hoechst and Cytotox Green are both nuclear stains, the overlap of Green Area or Green Intensity
301 (relative fluorescence units; RFU) with Hoechst allowed for intra-well normalization to study
302 varying levels of cell death from the chemotherapeutic treatment (Fig. 3A). Importantly, pairwise
303 comparison showed a strong correlation between BF and Hoechst normalized Green Area and
304 Green Intensity, thus making a fluorescent live-cell labelling dye (nuclear or cytoplasmatic)
305 redundant (Fig. 3B). Total Green Area / Total Mask Area resulted in the broadest dynamic range
306 (~Δ0.6 vs. ~Δ0.4), although a complete overlap (R = 1) in the 100 % cell death control (100 µM
307 CDDP) was not reached (Fig. 3B). Therefore, the proposed analysis provides an important
308 advantage by including intra-well, normalized organoid death, even without the use of a viability
309 label.

310 Overall, we showed that our OrBITS software can mask organoids with high accuracy ranging
311 from single cells to full-grown organoids based on BF imaging. In addition, inclusion of a
312 fluorescent cell death marker allowed for kinetic detection of intra-well normalized organoid
313 death. This allows for the removal of a nuclear or cytoplasmatic viability stain during kinetic
314 analysis, a key limitation of the current state-of-the-art analysis, as it can influence cellular growth
315 and health and confounds the effect of treatments.

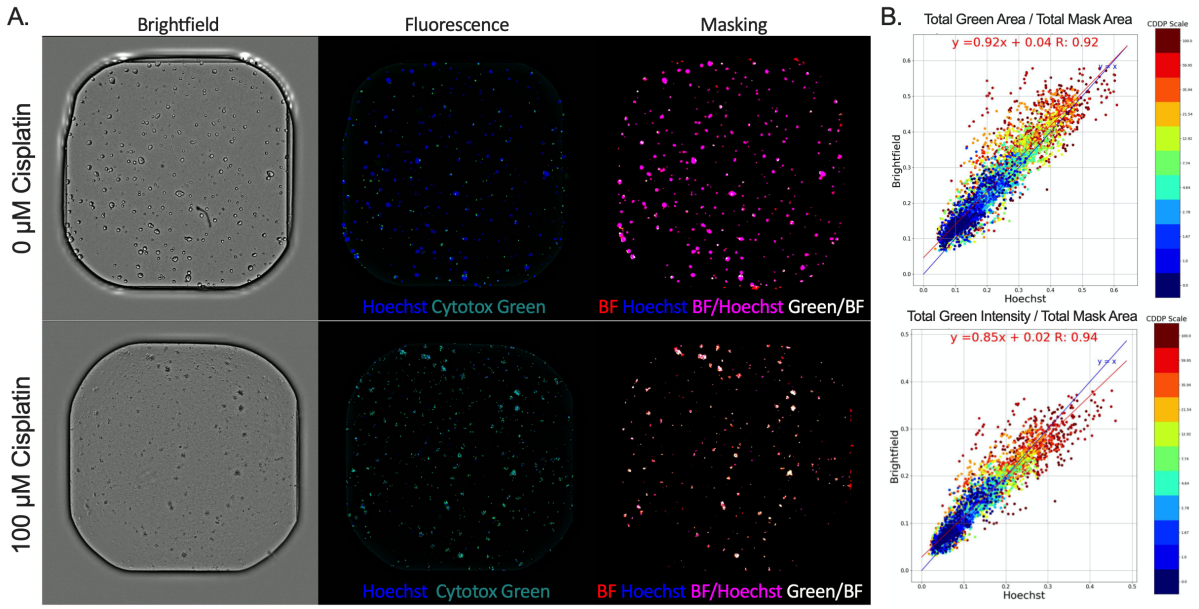

316

317 **Figure 3: Brightfield vs Hoechst normalized fluorescent cell death marker.** (A) Representative brightfield and
318 fluorescent (Hoechst and Cytotox Green) images of untreated and 100 µM cisplatin (CDDP) treated NSCLC_051T
319 PDOs and the corresponding masking of Brightfield, Hoechst, Brightfield/Hoechst overlap and Cytotox
320 Green/Brightfield overlap. (B) Pairwise comparison of Total Green Area / Total Mask Area (per well: $\mu m^2/\mu m^2$) and
321 Total Green Intensity / Total Mask Area (per well: RFU/ μm^2) with Mask Area based on either Hoechst fluorescence
322 imaging or BF imaging (Table S2). Blue line: line of unity (x=y), red line: best-fit linear regression.
323

324 **3.4 Validation of OrBITS brightfield PDO monitoring in proof-of-concept drug screening:**
325 **Comparison to CellTiter-Glo3D**

326 In order to determine if the OrBITS software could accurately monitor viability and therapy
327 response in PDOs, we compared the BF image analysis with the current industry and research

328 standard: CellTiter-Glo 3D viability assay. PDOs were again treated with a 10-point titration of
329 cisplatin, imaged and analyzed with both OrBITS and the CellTiter-Glo 3D viability assay, and
330 the read-outs were compared. Pairwise comparison revealed that the Total Mask Area had the
331 strongest correlation with the CellTiter-Glo 3D luminescent signal, since both parameters result
332 from whole-well readouts (Fig. 4A).
333 The assay quality was assessed based on the Z-factor, a coefficient reflective of both assay signal
334 dynamic range and data variation, using 100 μM cisplatin as positive control for NSCLC_051T.
335 The CellTiter-Glo 3D read-out was characterized by a Z-factor of 0.78 and the Total BF Area by
336 a Z-factor of 0.69, indicating that the BF assay is excellent for drug screening. When applying both
337 vehicle (100% viability; PBS) and baseline normalization (0% viability; 100 μM cisplatin) no
338 significant difference ($p = 0.0791$) was observed between IC50 values obtained by the Total BF
339 Area analysis and CellTiter-Glo 3D assay (Fig. 4B).
340 To validate our approach, we performed a drug screen of 6 standard-of-care lung cancer treatments
341 on an additional PDO line (NSCLC_013T) using 1 μM staurosporine as the standardized 100%
342 cell death control. A clear overlap of the inhibitory dose-response curves (Fig. 4C) and
343 corresponding IC50 values (Fig. S4) was observed between the Total Mask Area analysis and
344 CellTiter-Glo 3D assay. Therefore, it was clear that the OrBITS software could accurately monitor
345 PDOs for various anti-cancer drug screenings.

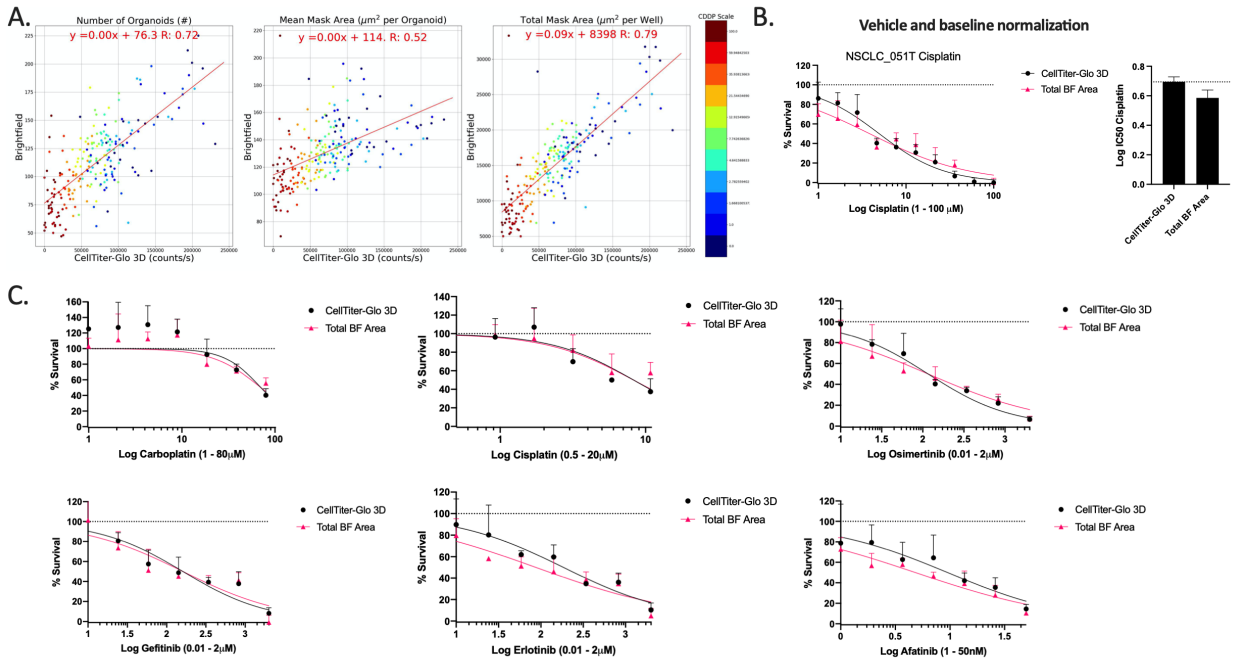

Figure 4: Brightfield imaging as a viability marker to monitor therapy response. (A) Pairwise comparison of organoid Count, Mean Mask Area and Total Mask Area with the luminescent read-out (counts/s) of the CellTiter-Glo 3D assay for the NSCLC_051T, NSCLC_051N, co-culture NSCLC_051T/N and NSCLC_050N PDO lines treated with a 10-point titration of cisplatin. Both read-outs were acquired at the same timepoint (114 hours) (Table S2). (B) Dose-response curve and corresponding IC50-values for NSCLC_051T treated with a 10-point titration of cisplatin and normalized to vehicle (100%) and baseline (0%, 100 µM cisplatin). (C) Dose-response curves of NSCLC_013T PDOs treated with a 7-point titration of cisplatin, carboplatin, erlotinib, gefitinib, osimertinib or afatinib normalized to vehicle (100%) and baseline (0%, 1 µM staurosporine). Corresponding IC50 values are presented in fig. S4. Graphs presented as mean ± SD of 5 technical replicates.

We observed that the Total BF Area resulted in an overestimation of the percentage of viable cells compared to the CellTiter-Glo 3D assay, when limiting normalization to the vehicle control (Fig. 5A-C). The difference increased with cisplatin concentration, which was not unexpected since dead organoids were still counted by BF imaging. Therefore, we used a fluorescent cell death marker (Cytotox Green or equivalent) to correct for the area covered by dead entities, thus producing the parameter Total BF Area – Total Green Area. This parameter was characterized by a Z-factor of 0.80 for the NSCLC_051T line and both the dose-response curves and IC50-values showed an improved overlap with the CellTiter-Glo 3D assay for NSCLC_051T, 051N/T (mixed

365 N and T) and 051N organoids (Fig. 5A-C). Importantly, the parameter showed a clear distinction
366 in sensitivity between the NSCLC_051T and NSCLC_051N lines, with an intermediate response
367 in the co-culture of both lines (Fig. 5D). In addition, this parameter allowed for kinetic monitoring
368 of cell viability (Fig. 5E) and vehicle-normalized survival (Fig. 5F), thus making early detection
369 of therapy response possible.
370 Overall, we demonstrated that the parameters used in our proposed BF image analysis were robust
371 and determined cell viability and IC50-values corresponding to the gold standard CellTiter-Glo
372 3D assay. Our OrBITS software is a significant advance from the current gold standard assay by
373 addressing its intrinsic limitations, as it allows for kinetic monitoring of organoid health and
374 growth from limited starting material and independent of metabolic changes.

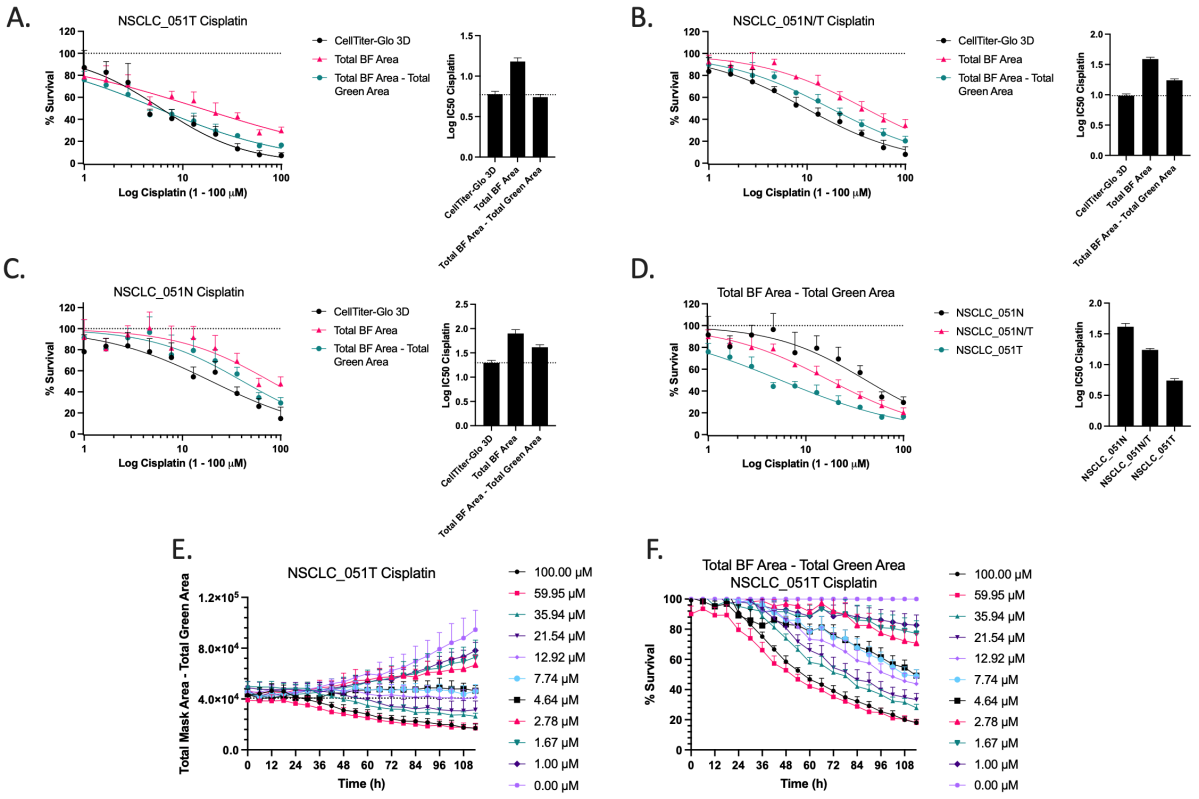

375

376 **Figure 5: Cell death corrected vehicle normalization.** (A-C) Dose-response curves and corresponding IC50-values
377 for NSCLC_051T, NSCLC_051N and co-culture NSCLC_051N/T treated with a 10-point titration of cisplatin and
378 normalized to vehicle (100%) control. Real-time monitoring of (E) cell viability and (F) survival percentage of
379 NSCLC_051T PDOs treated with a 10-point titration of cisplatin. Percent survival was baseline corrected to vehicle
380 control at each timepoint. Graphs presented as mean ± SD of 5 technical replicates.
381

382 **3.5 Validation of OrBITS analysis to delineate cytostatic and cytotoxic anti-cancer therapy**
383 **response**

384 The ATP-based PDO drug screening analysis method does not provide insight into the mechanistic
385 action of the drug, and therefore, we aimed to distinguish a cytostatic response (i.e. growth arrest)
386 from a cytotoxic response (i.e. cell death) using the OrBITS software. To achieve this, we
387 quantified the amount of therapy-induced organoid death using our BF and fluorescent image
388 analysis and the CellTiter-Glo 3D assay. Pairwise comparison showed an inverse correlation of
389 Total Green Area and Total Green Intensity normalized to Total BF Area with the CellTiter-Glo
390 3D readout (Fig. 6A). The assay quality was assessed based on the Z-factor using 100 µM cisplatin
391 as positive control for NSCLC_051T.Total Green Area / Total BF Area and Total Green Intensity
392 / Total BF Area were characterized by a Z-factor of 0.71 and 0.75, respectively, consistent with a
393 robust assay. A clear inverse relation was observed for the inhibitory dose-response curve (%
394 survival) and stimulatory dose-response curve of both the Total Green Area and Intensity
395 parameters normalized to BF area (% cell death) for cisplatin treated NSCLC_051T PDOs,
396 suggesting a cytotoxic response in this organoid line (Fig. 6B). An example of a cytostatic response
397 is given for NSCLC_013T treated with gefitinib (Fig. 6C). The use of Total Green Area was a
398 more standardized parameter since it was less susceptible to variability compared to the Total
399 Green Intensity parameter (e.g. led intensity, exposure time, and dye concentration). In addition to
400 delineating cytotoxic and cytostatic therapy responses, our method allowed for kinetic monitoring
401 of therapy-induced cell death (Fig. 6D) and assessment of organoid health (growth and viability)

as an imperative run quality control (Fig. 6E). Moreover, our method allowed for more in-depth research on the type of therapy-induced cell death that occurred. For example, cisplatin induced caspase 3/7 activity in NSCLC_046T, which is partly inhibited by the pan-caspase inhibitor Z-VAD-FMK (Fig. 6F). Consistently, Z-VAD-FMK inhibited cisplatin induced cell death, indicating that cytotoxicity occurs through caspase-dependent apoptosis (Fig. 6G). Here, the importance of kinetic monitoring is further highlighted, as the inhibitory effect of Z-VAD-FMK is nullified at 72h.

Overall, we demonstrated that OrBITS allowed for kinetic and endpoint analysis of therapy-induced cell death to distinguish cytostatic from cytotoxic responses and can be further developed to provide in-depth insight into the mechanistic action.

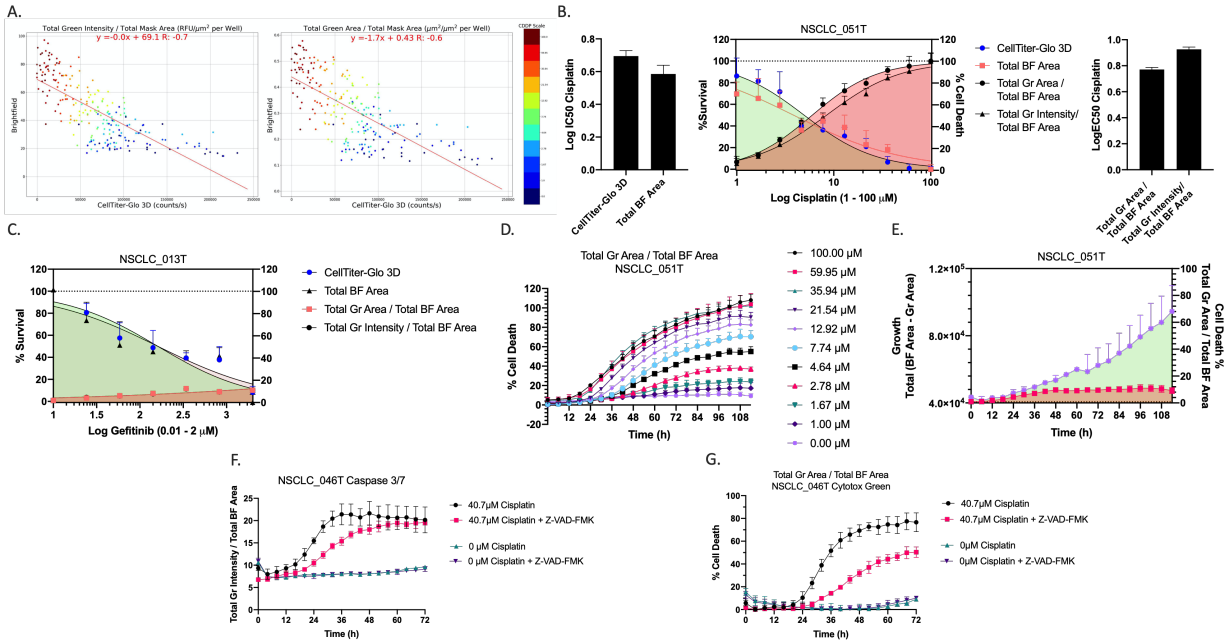

Figure 6: Fluorescent/brightfield imaging as a cell death marker. (A) Pairwise comparison of Total Green Intensity and Total Green Area (Cytotox Green reagent) normalized to Total BF Area with the luminescent read-out (counts/s) of the CellTiter-Glo 3D assay for the NSCLC_051T, NSCLC_051N, co-culture NSCLC_051T/N and NSCLC_050N PDO lines treated with a 10-point titration of cisplatin (Table S2). (B) Inhibitory (% survival, normalized to vehicle (100%) and baseline control (0%, 100 µM cisplatin) and stimulatory (% cell death, normalized to vehicle (0%) and positive control (100%, 100 µM cisplatin) dose-response curves and the corresponding IC50 and

419 EC50 values for NSCLC_051T PDOs treated with a 10-point titration of cisplatin. (C) Inhibitory (% survival,
420 normalized to vehicle (100%) and baseline control (0%, 1 µM staurosporine) and stimulatory (% cell death,
421 normalized to vehicle (0%) and positive control (100%, 1 µM staurosporine) dose-response curves NSCLC_013T
422 PDOs treated with a 7-point titration of gefitinib. (D) Real-time monitoring of therapy-induced cell death of
423 NSCLC_051T PDOs treated with a 10-point titration of cisplatin. Total Green Area / Total BF Area was normalized
424 to baseline (0%, vehicle at t = 0h) and positive (100%, 100 µM cisplatin at t = 72h) controls. (E) Real-time monitoring
425 of organoid growth (Total BF Area – Total Green Area) and cell death (Total Green Area / Total BF Area) as run
426 quality control. (F) Total Green Intensity / Total BF Area of the Caspase 3/7 green reagent in NSCLC_046T PDOs
427 treated with cisplatin +/- Z-VAD-FMK (pan-caspase inhibitor). (G) Percentage of cell death of NSCLC_046T
428 organoids treated with cisplatin +/- Z-VAD-FMK. Total Green Area / Total BF Area was normalized to baseline (0%,
429 lowest value) and positive (100%, 75 µM cisplatin at t = 72h) controls. Graphs presented as mean ± SD of 5 technical
430 replicates.

431 **3.6 The normalized drug response metric improves patient stratification.**

432 Inter-patient differences in PDO growth rate and experimental artifacts like variations in inter-well
433 seeding densities can lead to biased drug response estimates. Growth rate-based metrics correct
434 for these variations and our method allows for the quantification of intra-well growth rate over
435 time. When comparing the GR (negative control, fig. 7A) and NDR (positive and negative control,
436 fig. 7B) metrics to the cell death percentage of cisplatin-treated NSCLC_051T PDOs, we identified
437 that the NDR calculated from Total BF Area – Total Green Area most accurately resembles the
438 cytotoxic response. In addition, the NDR (Fig. 7D) improved the separation between gemcitabine
439 drug response from two PDAC PDOs compared to GR (Fig. 7C), which more accurately
440 represented the clinical response of the patients treated with neoadjuvant gemcitabine-paclitaxel
441 since PDAC_052 had a prolonged clinical response compared to PDAC_060 (disease control of 1
442 year vs. 4 months). The potential value of our method and the use of the NDR metric for improved
443 therapy response prediction is currently being validated in a larger cohort of patients.

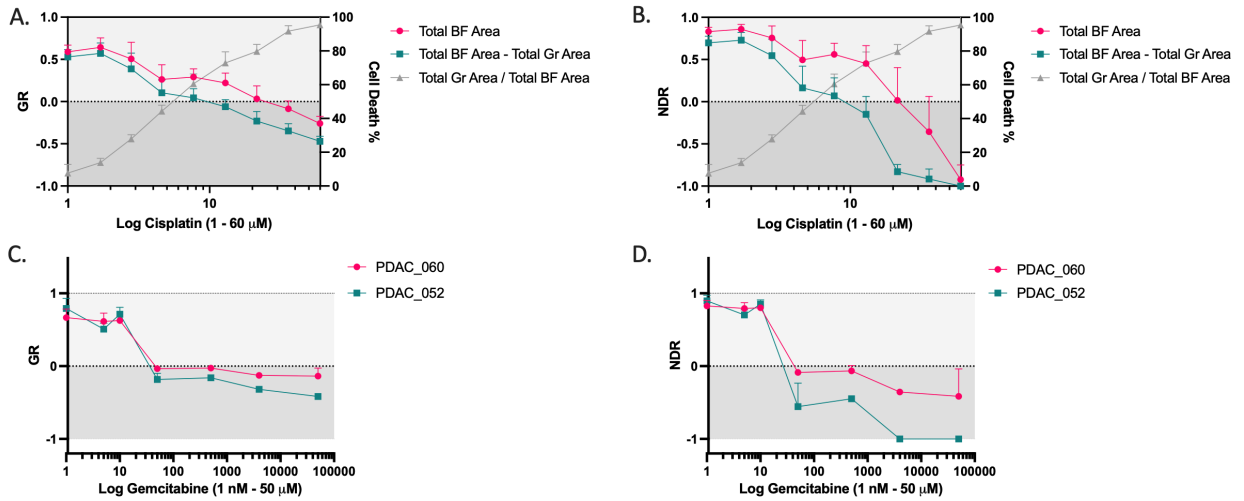

Figure 7: Growth Rate (GR) and normalized drug response (NDR) metrics. (A) NSCLC_051T treated with a 9-point titration of cisplatin. Left y-axis: GR (t = 120h) normalized to vehicle control. Right y-axis: % cell death, normalized to vehicle (0%) and positive (100%, 100 μM cisplatin) control. (B) NSCLC_051T treated with a 9-point titration of cisplatin. Left y-axis: NDR (t = 120h) normalized to vehicle and positive (100 μM cisplatin) control. Right y-axis: % cell death, normalized to vehicle (0%) and positive control (100%, 100 μM cisplatin). PDAC_060 and PDAC_052 treated with a 7-point titration of gemcitabine and (C) GR and (D) NDR calculated from Total BF Area – Total Green Area and normalized to vehicle control and vehicle and positive control (2 μM staurosporine), respectively.

3.7 Broad applicability of OrBITS for various organoid platforms and cancer cell lines

While the OrBITS software was developed using lung organoids in a high-throughput 384-well plate format, we have also successfully implemented the image analysis method for a range of cancer cell lines and PDOs of other tumor types. For example, we demonstrated the precise tracking capability on the growth of 3 cell lines (NCI-H1975, HCT-15, and NCI-H460) and pancreatic cancer-derived organoids using BF imaging (Supplemental Video 4). An overview off compatible cell lines we have tested to date is provided in table S3. Furthermore, we demonstrated that OrBITS is able to accurately mask organoids in other platforms. Pancreatic cancer organoids embedded in extracellular matrix domes were successfully monitored with OrBITS (Fig. 8A, Supplemental Video 5). This is highly advantages as it allows for monitoring of routine organoid

465 cultures and long-term screening assays in various culture plate. OrBITS BF image analysis was
466 also tested on the Gri3D®-96 well plates, an organoid plate format with hydrogel-based
467 microcavities for high-throughput organoid cultures(19). Impressively, OrBITS accurately
468 discriminated organoids from background in the BF images without additional training of the
469 convolutional neural network (Fig. 8B, Supplemental Video 6). Taken together, it is clear that
470 OrBITS analysis is not limited to a certain cell culture plate or culturing method, but can broadly
471 be applied to fit various research needs.
472 Lastly, for broad applicability of the OrBITS analysis software, it was also crucial to demonstrate
473 that it could be used on different image capturing systems. Therefore, the neural network was
474 trained on images obtained with the Spark Cyto 600 system (Tecan), we also assessed its ability
475 for masking with images acquired by the IncuCyte S3 (Sartorius). NCI-H460 lung cancer cells
476 were grown as multispheroids and imaged with a 4x objective in phase-contrast. OrBITS was once
477 again able to accurately mask the multispheroids and provide kinetic growth monitoring (Fig. 8C,
478 Supplemental Video 7), thus indicating that the OrBITS analysis software is not limited to a single
479 image capturing instrument.
480 Overall, we showed that the OrBITS software has broad applicability, in terms of various cell and
481 organoid types, imaging systems and culturing methods, ranging from conventional to state-of-the
482 art.

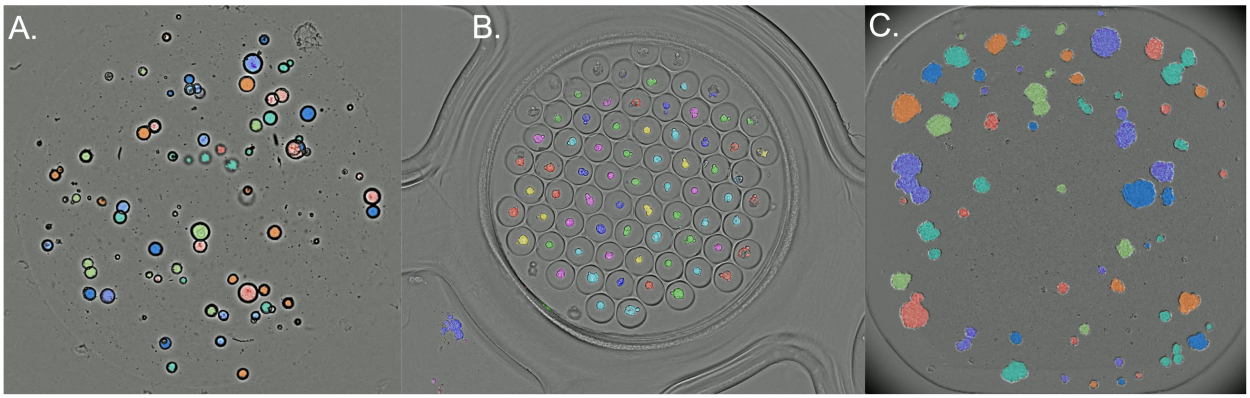

Figure 8: Examples of the broad applicability of OrBITS. (A) Cystic pancreatic cancer organoids (PDAC_060) grown in an extracellular matrix dome. Kinetic growth monitoring is shown in supplemental video 5. **(B)** Cancer cell line spheroids grown in a Gri3D®-96 well plate. Kinetic growth monitoring is shown in supplemental video 6. **(C)** NCI-H460 lung cancer cells grown as multispheroids and imaged with a 4x objective, phase-contrast using an IncuCyte S3 (Sartorius). Kinetic growth monitoring following treatment with cisplatin is shown in supplemental video 7. Colors indicate if connected objects are segmented individually (different colors), or as one object (same color).

4. Discussion

In this study we validated a new brightfield imaging-based method for ex vivo drug screening on patient-derived organoids. The Spark Cyto 600 system used here is a state-of-the art multimode plate reader with BF and fluorescence imaging capabilities. With full environmental controls (e.g. O_2, CO_2, temperature) and an injector, we automated the system to plate single cells or full-grown organoids, perform kinetic measurements, and dispense reagents (e.g. CellTiterGlo-3D) for endpoint analysis. This greatly improves the organoid culture by reducing variability involved with the cumbersome manual cultures, particularly in 384-well plates. While this all-in-one system ideal for the clinical implementation of drug sensitivity screens on patient-derived tumor organoids, the current limitation is the Spark Cyto Image Analyzer software, which is limited to 2D analysis. Therefore, we developed a deep learning image analysis solution OrBITS for 3D organoid/spheroid segmentation based on BF images.

504 Our system identifies organoids from BF images, thus removing the need for nuclear or
505 cytoplasmatic fluorescent labeling, which can affect biological process and confound therapy
506 responses. As demonstrated, there are several benefits to using the BF channel to detect and
507 measure organoids over transient or stably expressed fluorescent markers. These include: (i) the
508 ability to detect organoids in cases where high cell death reduces detectability via nuclear markers;
509 (ii) increased reproducibility since variance related to dye concentrations, stability (e.g.
510 photobleaching), LED intensity, and exposure time is removed; (iii) the ability to detect cystic
511 organoids, which can be problematic since Hoechst only stains the outer edge of cystic organoids;
512 (iv) optimal size and growth metrics, since it is not guaranteed that all parts of the organoid object
513 will contain viable nucleated cells as organoids grow, and therefore, reliance of fluorescent
514 markers therefore must be limited; (v) the ability to distinguish valid organoids from artifacts such
515 as cellular debris which may produce false positives or bubbles which may occlude cells; (vi) and
516 lastly, the reduction of any interfering effects of repeated fluorescence imaging on growth and
517 metabolism due to the release of reactive oxygen species by photoexcited fluorophores and other
518 side-effects related to phototoxicity (20).
519 Without the need to consider cytotoxic interference, imaging can be performed at higher frequency
520 time intervals. This opens up new possibilities for studies into how drugs affect organoid growth
521 and migration over time, which is currently not possible with simple endpoint assays. A key
522 measurement parameter of drug screening studies is cell viability. This is commonly done using
523 CellTiter-Glo 3D which, as an endpoint assay, is highly constrained. Alternatives to CellTiter-Glo
524 3D for measurement of cell death and viability are especially welcomed, since several therapies
525 are known to affect the primary parameter of measurement for CellTiter-Glo 3D (ATP) via

526 modulating intracellular ATP levels or releasing extracellular ATP following (immunogenic) cell
527 death (21). Furthermore, this approach does not distinguish cytotoxic from cytostatic responses,
528 which could further improve translatability of drug responses to the clinic and requires further
529 investigation.
530 Using our method, we demonstrated that organoids can be grown from either single-cells or full-
531 grown organoids with equal efficiency in 384-well plates. Gao et. al recently demonstrated that
532 organoids starting from single-cells demonstrated similar sensitivity to cytotoxic drugs to matched
533 full grown organoids (22). However, we recommend plating full grown organoids or at least delay
534 treatment until multicellular organoids have been grown from the single cells. By using live-cell
535 imaging, our method can greatly reduce turn-around time for *ex vivo* drug screenings as OrBITS
536 can accurately monitoring organoid growth, health and therapy response with a limited amount of
537 starting material on a single organoid level (13). In addition, kinetic imaging allows for early
538 detection of therapy response and the use of growth rate metrics has been shown to result in higher
539 reproducibility via uncoupling the effect of cell proliferation on drug sensitivity (14, 23). In
540 contrast to CellTiter-Glo 3D, growth rates can be calculated for each well individually to reduce
541 variations caused by seeding density. The use of a positive and negative control and the normalized
542 drug response, as developed by Gupta and colleagues, resulted in the best discrimination in
543 gemcitabine drug response between two PDAC patients with varying clinical outcomes following
544 neoadjuvant gemcitabine-paclitaxel treatment. A larger study is currently ongoing in our group to
545 support our hypothesis that the combination of live-cell imaging, OrBITS image analysis and the
546 normalized drug response metric can improve stratification of patients into responders and non-
547 responders.

548 Here, we demonstrated organoid identification, growth, and death using BF images, but we have
549 only begun to tap into the potential of BF image analysis. In principle, other morphological
550 changes with clinical and research implications are currently being pursued for organoids, 3D
551 spheroid cultures, and 2D monolayers. We also demonstrated the flexibility of the OrBITS
552 platform to differing culture methods, ranging from conventional (e.g. well-plates, matrix domes)
553 to state-of-the-art (Gri3D®-96), and imaging systems (SparkCyto 600 and IncuCyte S3).
554 Furthermore, we demonstrate the analysis capability on various cell and organoids lines apart from
555 those used for developing the BF imaging software. In the process, we confirmed the challenges
556 related to establishing lung cancer organoids as described by Dijkstra et al. (18). A more minimal
557 medium compared to the one used in this study has recently been described which should limit the
558 growth of normal lung organoids (24), although we observed no sustained organoid growth tested
559 in a small set of samples. The use of Napsin A, p63 or p40 (ΔNp63) and TTF-1 allows for
560 identifying cultures overgrown by non-malignant lung cells. As such, the patient-derived
561 organoids used in our method development were non-malignant organoids displaying either a solid
562 (derived from tumor tissue) or cystic (derived from healthy tissue) growth pattern. Apart from the
563 clear difference in morphology, the non-malignant organoids derived from tumor tissue
564 (NSCLC_051T) were more sensitive to cisplatin compared to the organoids derived from healthy
565 tissue from the same patient (NSCLC_051N). This further indicates that these cells have different
566 characteristics which could influence the outcome of a drug sensitivity screen if present in tumor
567 organoid cultures. Even so, our method is also be applicable in tumor organoids as shown for
568 PDAC organoids (18, 24).

569 **5. Conclusions**

570 We demonstrated that our in-house developed OrBITS image analysis software can monitor PDOs
571 with high accuracy ranging from single cells to full-grown organoids based on BF imaging.
572 Inclusion of a fluorescent cell death marker allowed for real-time monitoring of intra-well
573 normalized organoid death. When validated against the current gold standard CellTiter-Glo 3D
574 assay, the OrBITS imaging analysis was robust in determining cell viability, IC50-values.
575 Furthermore, we demonstrated that OrBITS could distinguish cytostatic from cytotoxic responses
576 most accurately by the inclusion of a fluorescent cell death marker and the use of the normalised
577 drug response metric to provide more in-depth insight into anticancer drug mechanisms. Combined
578 with providing high-throughput, kinetic monitoring of PDOs, OrBITS is a significant advance
579 from the current state-of-the-art analysis technique made available for mid-end live-cell imaging
580 instruments, which are often simple, endpoint analysis, or provide no mechanistic insights. Taken
581 together, OrBITS, as a scalable, high-throughput technology, would facilitate the use of PDOs for
582 drug development, therapy screening, and guided clinical decisions for personalized medicine. The
583 developed platform also provides a launching point for further brightfield-based assay
584 development to be used for fundamental research.

585 **List of Abbreviations**

586 OrBITS: Organoid Brightfield Identification-based Therapy Screening

587 PDOs: Patient-derived organoids

588 BF: Brightfield

589 NSCLC: Non-small cell lung carcinoma

590 UZA: Antwerp University Hospital

591 RFU: Relative fluorescence units

592 **Declarations**

593 **Ethics approval and consent to participate**

594 Written informed consent were obtained from all patients, and the study was approved by the UZA
595 Ethical Committee (ref. 17/30/339, 14/47/480).

596 **Consent for publication**

597 All co-authors have read and approved of its submission to this journal and no individual person's
598 data is used.

599 **Availability of data and materials**

600 The datasets used and/or analyzed during the current study are available from the corresponding
601 author on reasonable request.

602 **Competing interests**

603 The authors declare that they have no competing interests.

604 **Funding**

605 This work was funded in part by the Flanders Research Foundation, 12S9221N (A.L.),
606 12S9218N (A.L.), G044420N (A.B., S.V., A.L.) and by the Industrial Research Fund of the
607 University of Antwerp, PS ID 45151 (C.D., S.V., A.L.).

608 **Authors contribution**

609 C.D, E.C.DLH. and A.L. conceived the idea and wrote the manuscript. C.D., M.L.C. performed
610 the in vitro experiments. E.C.DLH. developed the software and analyzed the data. P.V.S., J.M.H,

611 P.L, S.K.Y supplied the patient derived materials. F.L, P.P, A.B, E.S., A.L. substantially revised
612 the manuscript.

613 **Acknowledgements**

614 We would like to thank Mr. Willy Floren for funding the D300e and Tecan for gifting the Spark
615 Cyto as part of a competition.

616 **References**

617 1. Drost J, Clevers H. Organoids in cancer research. Nat Rev Cancer. 2018;18(7):407-18.
618 2. Narasimhan V, Wright JA, Churchill M, Wang T, Rosati R, Lannagan TRM, et al. Medium-
619 throughput Drug Screening of Patient-derived Organoids from Colorectal Peritoneal Metastases to Direct
620 Personalized Therapy. Clinical cancer research : an official journal of the American Association for Cancer
621 Research. 2020.
622 3. Ooft SN, Weeber F, Dijkstra KK, McLean CM, Kaing S, van Werkhoven E, et al. Patient-derived
623 organoids can predict response to chemotherapy in metastatic colorectal cancer patients. Science
624 translational medicine. 2019;11(513).
625 4. Driehuis E, van Hoeck A, Moore K, Kolders S, Francies HE, Gulersonmez MC, et al. Pancreatic
626 cancer organoids recapitulate disease and allow personalized drug screening. Proceedings of the National
627 Academy of Sciences of the United States of America. 2019.
628 5. Driehuis E, Spelier S, Beltran Hernandez I, de Bree R, S MW, Clevers H, et al. Patient-Derived Head
629 and Neck Cancer Organoids Recapitulate EGFR Expression Levels of Respective Tissues and Are Responsive
630 to EGFR-Targeted Photodynamic Therapy. J Clin Med. 2019;8(11).
631 6. Driehuis E, Kolders S, Spelier S, Lohmussaar K, Willems SM, Devriese LA, et al. Oral Mucosal
632 Organoids as a Potential Platform for Personalized Cancer Therapy. Cancer discovery. 2019;9(7):852-71.
633 7. Vlachogiannis G, Hedayat S, Vatsiou A, Jamin Y, Fernandez-Mateos J, Khan K, et al. Patient-derived
634 organoids model treatment response of metastatic gastrointestinal cancers. Science.
635 2018;359(6378):920-6.
636 8. Nagle PW, Plukker JTM, Muijs CT, van Luijk P, Coppes RP. Patient-derived tumor organoids for
637 prediction of cancer treatment response. Seminars in cancer biology. 2018;53:258-64.
638 9. Choi YM, Kim HK, Shim W, Anwar MA, Kwon JW, Kwon HK, et al. Mechanism of Cisplatin-Induced
639 Cytotoxicity Is Correlated to Impaired Metabolism Due to Mitochondrial ROS Generation. PloS one.
640 2015;10(8):e0135083.
641 10. Shirmanova MV, Druzhkova IN, Lukina MM, Dudenkova VV, Ignatova NI, Snopova LB, et al.
642 Chemotherapy with cisplatin: insights into intracellular pH and metabolic landscape of cancer cells in vitro
643 and in vivo. Sci Rep. 2017;7(1):8911.
644 11. Zhou Y, Tozzi F, Chen J, Fan F, Xia L, Wang J, et al. Intracellular ATP levels are a pivotal determinant
645 of chemoresistance in colon cancer cells. Cancer research. 2012;72(1):304-14.
646 12. Ivanov DP, Grabowska AM. Spheroid arrays for high-throughput single-cell analysis of spatial
647 patterns and biomarker expression in 3D. Sci Rep. 2017;7:41160.

648 13. Le Compte M, Cardenas De La Hoz E, Peeters S, Smits E, Lardon F, Roeyen G, et al. Multiparametric
649 tumor organoid drug screening using widefield live-cell imaging for bulk and single-organoid analysis.
650 Journal of Visualized Experiments. 2022, under revision.
651 14. Hafner M, Niepel M, Chung M, Sorger PK. Growth rate inhibition metrics correct for confounders
652 in measuring sensitivity to cancer drugs. Nat Methods. 2016;13(6):521-7.
653 15. Gupta A, Gautam P, Wennerberg K, Aittokallio T. A normalized drug response metric improves
654 accuracy and consistency of anticancer drug sensitivity quantification in cell-based screening. Commun
655 Biol. 2020;3(1):42.
656 16. Zhang JH, Chung TD, Oldenburg KR. A Simple Statistical Parameter for Use in Evaluation and
657 Validation of High Throughput Screening Assays. J Biomol Screen. 1999;4(2):67-73.
658 17. Turner BM, Cagle PT, Sainz IM, Fukuoka J, Shen SS, Jagirdar J. Napsin A, a new marker for lung
659 adenocarcinoma, is complementary and more sensitive and specific than thyroid transcription factor 1 in
660 the differential diagnosis of primary pulmonary carcinoma: evaluation of 1674 cases by tissue microarray.
661 Arch Pathol Lab Med. 2012;136(2):163-71.
662 18. Dijkstra KK, Monkhorst K, Schipper LJ, Hartemink KJ, Smit EF, Kaing S, et al. Challenges in
663 Establishing Pure Lung Cancer Organoids Limit Their Utility for Personalized Medicine. Cell Rep.
664 2020;31(5):107588.
665 19. Brandenberg N, Hoehnel S, Kuttler F, Homicsko K, Ceroni C, Ringel T, et al. High-throughput
666 automated organoid culture via stem-cell aggregation in microcavity arrays. Nat Biomed Eng.
667 2020;4(9):863-74.
668 20. Icha J, Weber M, Waters JC, Norden C. Phototoxicity in live fluorescence microscopy, and how to
669 avoid it. Bioessays. 2017;39(8).
670 21. Krysko DV, Garg AD, Kaczmarek A, Krysko O, Agostinis P, Vandenabeele P. Immunogenic cell death
671 and DAMPs in cancer therapy. Nat Rev Cancer. 2012;12(12):860-75.
672 22. Gao M, Harper MM, Lin M, Qasem SA, Patel RA, Mardini SH, et al. Development of a Single-Cell
673 Technique to Increase Yield and Use of Gastrointestinal Cancer Organoids for Personalized Medicine
674 Application. J Am Coll Surg. 2020.
675 23. Driehuis E, Kretzschmar K, Clevers H. Establishment of patient-derived cancer organoids for drug-
676 screening applications. Nat Protoc. 2020;15(10):3380-409.
677 24. Kim M, Mun H, Sung CO, Cho EJ, Jeon HJ, Chun SM, et al. Patient-derived lung cancer organoids
678 as in vitro cancer models for therapeutic screening. Nature communications. 2019;10(1):3991.

679